RESEARCH

HDAC6 inhibition disrupts HDAC6-P300 interaction reshaping the cancer chromatin landscape

Michela Gottardi Zamperla[1†], Barbara Illi[2†], Veronica Barbi[1], Chiara Cencioni[3], Daniele Santoni[3], Stella Gagliardi[4], Maria Garofalo[4], Gabriele Antonio Zingale[5], Irene Pandino[5], Diego Sbardella[5], Lina Cipolla[6], Simone Sabbioneda[6], Antonella Farsetti[3], Chiara Ripamonti[7], Gianluca Fossati[7], Christian Steinkühler[7], Carlo Gaetano[1*] and Sandra Atlante[3]

Abstract

Background Histone deacetylases (HDACs) are crucial regulators of gene expression, DNA synthesis, and cellular processes, making them essential targets in cancer research. HDAC6, specifically, influences protein stability and chromatin dynamics. Despite HDAC6's potential therapeutic value, its exact role in gene regulation and chromatin remodeling needs further clarification. This study examines how HDAC6 inactivation influences lysine acetyltransferase P300 stabilization and subsequent effects on chromatin structure and function in cancer cells.

Methods and results We employed the HDAC6 inhibitor ITF3756, siRNA, or CRISPR/Cas9 gene editing to inactivate HDAC6 in different epigenomic backgrounds. Constantly, this inactivation led to significant changes in chromatin accessibility, particularly increased acetylation of histone H3 lysines 9, 14, and 27 (ATAC-seq and H3K27Ac ChIP-seq analysis). Transcriptomics, proteomics, and gene ontology analysis revealed gene changes in cell proliferation, adhesion, migration, and apoptosis. Significantly, HDAC6 inactivation altered P300 ubiquitination, stabilizing P300 and leading to downregulating genes critical for cancer cell survival.

Conclusions Our study highlights the substantial impact of HDAC6 inactivation on the chromatin landscape of cancer cells and suggests a role for P300 in contributing to the anticancer effects. The stabilization of P300 with HDAC6 inhibition proposes a potential shift in therapeutic focus from HDAC6 itself to its interaction with P300. This finding opens new avenues for developing targeted cancer therapies, improving our understanding of epigenetic mechanisms in cancer cells.

Keywords HDAC, HAT, Deacetylase inhibitors, Cancer, Tumorigenesis, Histone acetylation, Cell cycle, Proliferation, Apoptosis

---

[†]Michela Gottardi Zamperla and Barbara Illi have contributed equally to this work.

*Correspondence:
Carlo Gaetano
carlo.gaetano@icsmaugeri.it
Full list of author information is available at the end of the article

Zamperla *et al. Clinical Epigenetics*   (2024) 16:109

Page 2 of 20

Introduction

Histone deacetylases (HDACs) regulate gene expression, DNA synthesis, and cellular metabolism. Among these, histone deacetylase 6 (HDAC6) stands out for its unique structure and diverse cellular functions. As a class IIb HDAC, HDAC6 has two deacetylation catalytic domains. Additionally, it has a zinc-finger ubiquitin-binding domain (ZnF-UBP) [1]. This combined structure allows HDAC6 to deacetylate various substrates, including α-tubulin [2], cortactin [3], titin [4], and Hsp90 [5]. HDAC6 can also bind specific sequences on unanchored ubiquitin, acting as a carrier to transport aggregated proteins for degradation [3, 6–9]. While HDAC6 does not directly add ubiquitin chains to proteins, it interacts with E3 ligases and influences ubiquitination through regulatory functions [10, 11].

In addition to its established cellular roles [12], HDAC6 influences immune regulation, inflammation, and the response to viral infection. It contributes to inflammasome assembly and activation by modulating microtubule transport within cells [13]. Interestingly, some viruses may utilize HDAC6 during their infection cycle, potentially for the uncoating stage. In some cases, HDAC6 can act non-enzymatically to hinder viral invasion and replication. This multifaceted nature of HDAC6 also suggests its involvement in viral infections [14, 15].

The transcriptional co-activator lysine acetyltransferase P300 plays diverse roles in cellular processes, including chromatin remodeling, gene expression, protein turnover, embryonic development, and cell proliferation [10, 16]. Levels of P300 within the cell are tightly regulated, and alterations in its concentration have been associated with various disease states [17, 18]. P300 can undergo post-translational modifications, including polyubiquitination and sumoylation near its bromodomain. These modifications may be more prevalent when P300 is unphosphorylated [10, 16, 19].

Several signaling pathways, including the p38 MAP kinase and the Ras pathways, can influence the stability or degradation of P300 [10, 20]. In addition, post-translational modifications like phosphorylation, acetylation, ubiquitination, and interactions with other proteins can also affect the subcellular localization of P300. These regulatory mechanisms, likely involving specific signaling molecules and protein–protein interactions, modulate P300's function as a transcriptional co-activator [16, 20, 21].

Research indicates that P300 interacts with histone deacetylase 6 (HDAC6) and acetylates it, reducing the deacetylase activity [22]. P300 also modulates gene expression by interacting with and directly regulating transcription factors like Sp1. These complex interactions highlight the intricacy of the acetylation and deacetylation processes within cells [6, 23, 24].

The interplay between histone acetyltransferases (HATs) and HDACs, often co-localized at regulatory regions of genes, is essential for controlling gene expression. Selective HDAC inhibitors offer a potential strategy to restore the disrupted acetylation balance in various diseases, including cancer, respiratory, ophthalmic, and cardiac conditions.

Notably, the selective inhibition of HDAC6 has demonstrated minimal cytotoxic effects in healthy cells and mice [22, 25]. Developing isoform-selective HDAC inhibitors enables targeted therapeutic applications in cancer, inflammatory, and infectious diseases [1, 26]. Due to its role in various diseases and potential therapeutic value, several small-molecule inhibitors specifically designed to block HDAC6 deacetylase activity have been created [27]. One promising compound, ITF3756, is a potent and selective HDAC6 inhibitor with a favorable pharmacokinetic profile, exhibiting low toxicity in both cell culture and animal models. The experimental evidence suggests that ITF3756 may potentially treat autoimmune diseases, support organ transplantation, or modulate the anticancer immune response by enhancing the function of regulatory T cells. [28, 29].

While the functional interaction between HDAC6 and P300 has been characterized, the specific consequences of this interaction remain an area of active investigation [11, 23, 24]. HDAC6 and P300 interplay may be relevant in various pathological conditions, and a deeper understanding of their function may offer potential cues for novel therapeutic interventions. This study confirms the impact of HDAC6 inhibition/inactivation on gene expression and cancer cell behavior. More importantly, it explores the potential of HDAC6 to modulate P300 expression and activity, a phenomenon that may provide—at least in part—the basis for the epigenomic changes resulting from selective HDAC6 inhibition in cancer cells [26].

Materials and methods

An extended Materials and Methods section is available as supplemental information.

Cell culture, treatment, and transfection

HCC1806 (CRL-2335, *Homo sapiens*, breast cancer), MDA-MB-231 (CRM-HTB-26, *Homo sapiens*, breast cancer), Jurkat (Clone E6-1, TIB-152, H*omo sapiens*, Acute leukemia, T-lymphocyte), MRC5 (CCL-171, *Homo sapiens*, fetal lung, fibroblast) and WI-38 (CCL-75, *Homo sapiens*, fetal lung, fibroblast) cell lines were purchased from ATCC; B16-F10 WT line and KO line for HDAC6 were purchased from genOwa (*Mus musculus*, skin

Zamperla *et al. Clinical Epigenetics*   (2024) 16:109

Page 3 of 20

melanoma, a mixture of spindle-shaped and epithelial-like cells). When required, cells were exposed to 1 μM ITF3756 for 16 h. DMSO was used as a vehicle. For transfection details see extended methods.

Crystal violet staining

After treatment, cells were fixed in fresh 2% paraformaldehyde (PFA) at room temperature (RT) for 20 min (min) and stained with 0,5% Crystal violet solution (methyl violet 10B or hexamethyl pararosaniline chloride, prepared in 20% methanol) at RT for 5 min, washed with phosphate-buffered saline (PBS) and dried for 30 min.

ELISA assays

Total HDAC and HAT activity were assayed on nuclear and cytoplasmic extracts obtained using the Nuclear Extraction Kit (ab113474, Abcam), following the manufacturer's instructions. Total HDAC activity was quantified using the HDAC Activity Assay Kit (colorimetric, ab1432, Abcam), and total HAT activity was quantified using the Histone Acetyltransferase Activity Assay Kit (colorimetric, ab65352, Abcam) according to the supplier protocols.

mRNA extraction and qRT-PCR

According to the manufacturer's instructions, RNA was extracted from approximately 1×10^6 cells using Tri-Reagent (Sigma). cDNA synthesis for quantitative real-time PCR (qRT-PCR) was retrotranscribed with Omniscript RT Kit (Qiagen). All reactions were performed in RT^2 SYBR Green ROX qPCR Mastermix (Qiagen), using the QIAquant 96 5plex (230 V) Device (Qiagen).

Immunoprecipitation and capillary electrophoresis

Cells were lysed in 20 mM Tris–HCl (pH 7.4), 50 mM NaCl, 1% NP40/IGEPAL, 2 mM EDTA, 0.01% SDS, supplemented with protease/phosphatase inhibitor (PI/PhI) mix and 2 mM DTT and protein concentration was determined by a BCA kit. 500 μg of the extract was immunoprecipitated by using 5 μg of anti-P300 (RbMAb, Abcam), anti-HDAC6 (MsMAb, Abcam), or anti-Flag (MsMAb, Abcam) and Dynabeads-Protein G magnetic beads system (Thermo Fisher Scientific).

Protein extraction from mice tissue

Samples were cut into small pieces with a scalpel and transferred into tubes. To each tube, two 3 mm Tungsten Carbide Beads (Qiagen) and Laemmli buffer supplemented with 100 nM Phenylmethanesulfonyl fluoride (PMSF, Merck), 100 μM Trichostatin A (TSA, Cabru-Cayman Chemical), and PI/PhI mix were added. Samples were loaded to TissueLyzer LT and shaken 3–6 times for

3 min at 50 Hz; after centrifugation, samples were heated at 95 °C and sonicated to avoid DNA interference.

Immunofluorescence staining

Treated/untreated HCC1806 cells and WT and KO_HDAC6 B16F10 cells were cultured in LabTek II chamber slides (Nunc, Biosigma) and fixed in 4% PFA (Merck) for 10 min, RT, and permeabilized with 0.1% Triton solution (Merck) for 30 min at RT. Samples were blocked in 5% BSA for 90 min, incubated overnight at 4 °C with primary antibodies, and 1 h at RT with secondary antibodies.

Proximity ligation assay (PLA)

MCR5 cells were transfected with hHDAC6-Flag-pcDNA3.1+(Aurogene) and treated with ITF3756 at 1 μM for 16 h. Cells were then fixed with 4% PFA for 15 min, RT, permeabilized with 0.5% Triton X-100 for 20 min at RT, and blocked with 3% BSA–PBS 0.1% Tween for 1 h at 37 °C. Next, samples were incubated with P300 (1:200, RbMAb, Abcam) and Flag (1:200, MsMAb, Abcam) for two h at 37 °C and washed with PLA Buffer A (Sigma), and a classic PLA reaction was performed by using the SIGMA Duolink Kit, according to the manufacturer instructions.

Proteasome assay

Vehicle- and ITF3756-treated samples were lysed in an osmotic buffer according to a standard procedure for isolating crude cell extracts [30], and protein concentration was determined by BCA assay. After that, 20 μg of proteins was incubated for 10 min at 37 °C with or without 1 μM epoxomicin, a potent and irreversible inhibitor of proteasome chymotrypsin-like activity (Boston Biochem, MA, USA). 75 μM Suc-LLVY-amc (Boston Biochem, MA, USA) was added, and the fluorescence released by proteasome cleavage was recorded in a Varioskan Lux spectrofluorometer ($\lambda_{exc.} = 340$ nm; $\lambda_{em.} = 440$ nm). Slopes for individual samples were calculated by subtracting that observed in the presence of epoxomicin.

Western blotting

Cells were lysed in Laemmli buffer 1X supplemented with 1 mM DTT. After that, 4–20% acrylamide pre-cast gels (Bio-Rad, Hercules, CA, USA) were used to separate proteins by SDS-PAGE. After separation, proteins were transferred to a HyBond-ECL nitrocellulose filter (Bio-Rad, Hercules, CA, USA) and probed with antibodies for several targets [31].

Assay for transposase-accessible chromatin (ATAC) sample preparation

B16F10 KO_HDAC6 and WT cells and ITF3756- and DMSO-treated Jurkat cells were cultured for 16 h and

Zamperla *et al. Clinical Epigenetics*   (2024) 16:109

Page 4 of 20

then treated for 30 min at 37 °C with 1X DNase buffer (200 units/mL in HBSS, 2.5 mM $MgCl_2$, 0.5 mM $CaCl_2$). About 10^5 cells were then cryopreserved in 50% FBS, 40% growth media, 10% DMSO, frozen, and sent to Active Motif (Carlsbad, CA, USA) for analysis.

ATAC sequencing and bioinformatics analysis

The paired-end 42 bp sequencing reads (PE42) generated by Illumina sequencing were mapped to the genome using the BWA algorithm with default settings ("bwa mem"). Only reads that passed the Illumina purity filter, aligned with no more than 2 mismatches, and mapped uniquely to the genome were used in the subsequent analysis. In addition, duplicate reads ("PCR duplicates") were removed. Genomic regions with high transposition/ tagging events were determined using the MACS3 peak calling algorithm.

Chromatin immunoprecipitation (ChIP) sample preparation

ITF3756- and DMSO-treated Jurkat cells and B16F10 KO_HDAC6 and WT cells were cultured for 16 h, then cross-linked with 1% formaldehyde solution (10 mM NaCl, 100 µM EDTA pH 8.0, 5 mM HEPES, pH 7.9) and quenched with 120 mM Glycine. Samples were then treated with 0.5% Igepal supplemented with 1 mM PMSF, pelleted, snap frozen, and sent to Actif Motif (Carlsbad, CA, USA) for H3K27Ac-ChIP-seq analysis (anti-H3K27Ac, Cat# 39133).

ChIP sequencing and bioinformatics analysis

ChIP samples were processed for sequencing, and the 75-nt single-end (SE75) sequence reads generated by Illumina sequencing were mapped to the genome using the BWA algorithm ("bwa aln/samse" with default settings). Only reads that passed the Illumina purity filter, aligned with no more than 2 mismatches, and mapped uniquely to the genome were used in the subsequent analysis. In addition, duplicate reads ("PCR duplicates") were removed. Since the 5′-ends of the aligned reads (="tags")

represent the end of ChIP/IP-fragments, the tags were extended in silico (using Active Motif software) at their 3′-ends to a length of 200 bp, which corresponds to the average fragment length in the size-selected library.

Bioinformatics analysis of NGS studies

Volcano plots were computed using GraphPad Prism 8 to identify regions of interest in the ATAC-seq (Differentially accessible regions vs Differentially inaccessible regions) and the ChIP-seq (upregulated H3K27Ac targeted regions *vs* downregulated H3K27Ac targeted regions) applying the following threshold to identify statistically significant regions modulated by pharmacological treatment or HDAC6 KO: ±1 log2 fold change, fdr < 0.05. Data have been deposited in GEO under accession numbers GSE273644 and GSE273645.

RNA Library preparation, sequencing, and bioinformatics analysis

Sequencing libraries were prepared with the Illumina TruSeq Stranded RNA Library Prep, version 2, Protocol D, using 500-ng total RNA (Illumina). 4200 Tape Station assessed the quality of each library with a "DNA High sensitivity" assay (Agilent). Libraries were fluorometrically quantified using a Sensitivity dsDNA assay with a Qubit device (Life Technologies). The sequencing step was performed with NGS technologies using Illumina Genome Analyzer and the NextSeq 500/550 High Output v2.5 kit (150 cycles, Illumina), processed on Illumina NextSeq 500. FastQ files were generated via Illumina bcl2fastq2, version 2.17.1.14. Available online: http://support.illumina.com/downloads/ bcl-2fastq-conversion-software-v217.html (accessed on 2 May 2018, starting from raw sequencing reads produced by Illumina NextSeq sequencer). Pathway Analysis: Gene enrichment analysis was performed on coding genes. A Gene Ontology (GO) analysis was conducted for biological processes, cellular components, and molecular function, while KEGG pathway analysis (Kyoto Encyclopedia of Genes and Genomes available online: https://

(See figure on next page.)

Fig. 1 HDAC6 inhibitor ITF3756 and HDAC6 inactivation by CRISPR/CAS9 modulate lysine acetylation. **A**, **B** Immunofluorescence staining after ITF3756 treatment of HCC1806 cell line. Left: representative images showing the acetylation of H3K27 (**A**) and H3K9 (**B**) (green signal) after 16 h treatment with ITF3756 1 µM. DAPI (blue signal) and α-Tubulin (red signal) were used as normalizers. Images were acquired at 20X magnification. Scale bar: 100 µm. Right: densitometric analysis of the mean fluorescent intensity (MFI) of the ITF3756-treated cells (green bar) compared to solvent (black bar). Error bars indicate SEM. Data were analyzed by paired *t* test, $N = 3$; *$p < 0.05$; **$p < 0.005$. **C**, **D** Immunofluorescence staining of B16F10 KO_HDAC6 *vs* WT. Left: representative images showing the acetylation of H3K27 (**C**) and H3K9 (**D**) (green signal). DAPI (blue signal) and α-Tubulin (red signal) were used as normalizers. Images acquired at 40X magnification. Scale bar: 50 µm. Right: densitometric analysis of the mean fluorescent intensity (MFI) of the KO_HDAC6 condition (green bar) compared to the control (black bar). Error bars indicate SEM. Data were analyzed by unpaired *t* test, $N = 3$; *$p < 0.05$; **$p < 0.005$. **E**, **F** The graphs show the results of capillary electrophoresis experiments performed to detect H3K9 and H3K27 acetylation in the liver (**E**) and spleen (**F**) of HDAC6_KO mice (blue dots) compared to the control (WT, black dots). The β-Actin was used as a normalizer. Error bars indicate SD. Data were analyzed by unpaired *t* test, $N = 10$ for each condition; *$p < 0.05$
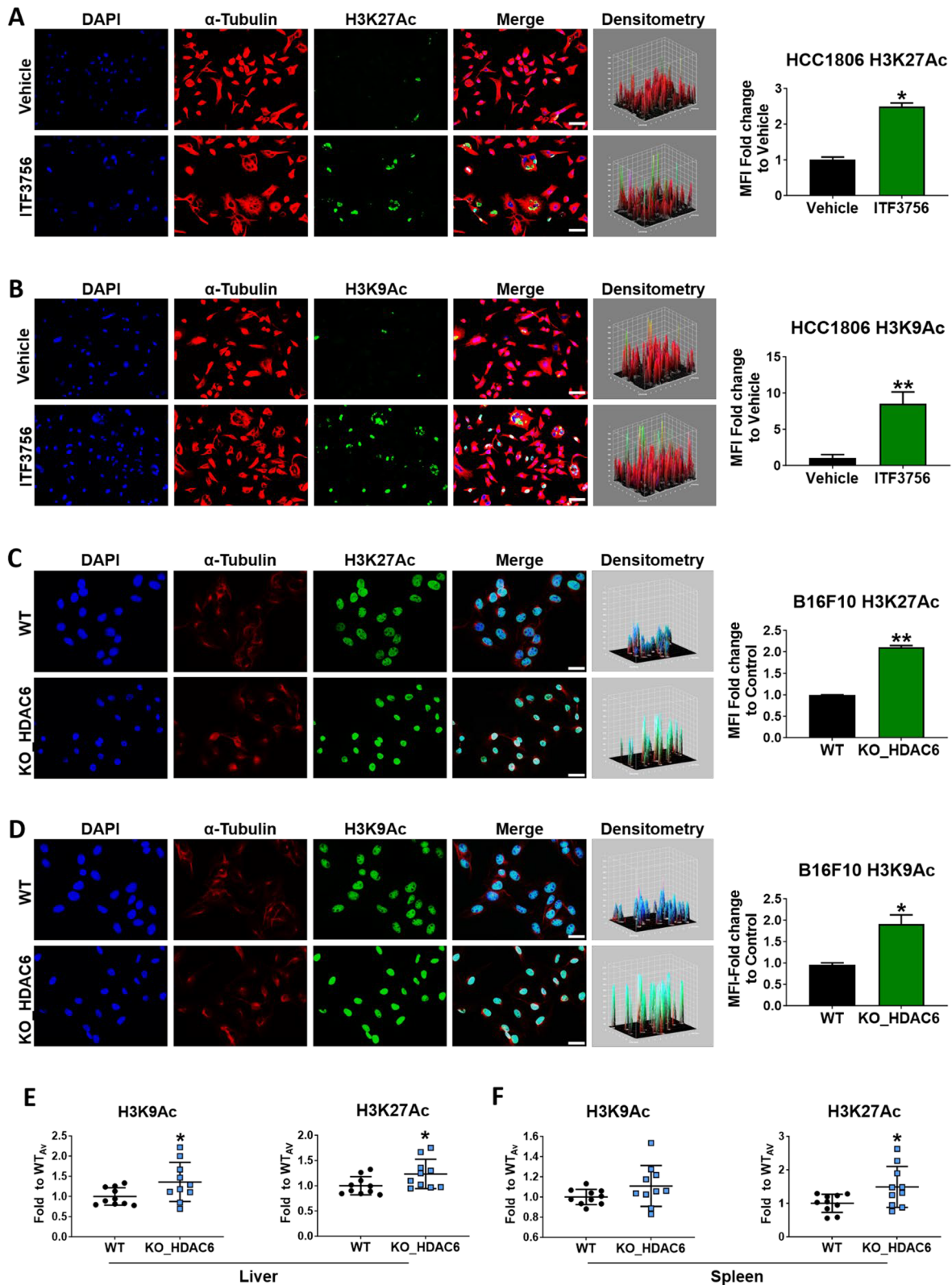
Fig. 1 (See legend on previous page.)

Zamperla *et al. Clinical Epigenetics*   (2024) 16:109

Page 6 of 20

www.genome.jp/kegg/pathway.html; accessed on 2 May 2018) was conducted for pathway analysis. For this investigation, we used the enrichR web tool (accessed on 10 December 2019).

Proteomics studies

The proteome characterization of HDAC6-silenced and scrambled (treated with a non-targeting pool of siRNA) HCC1806 cells was performed using a standard shot-gun proteomics protocol. Peptides were analyzed by LC/MS−MS in Orbitrap Exploris 240 (Thermo Fisher Scientific, Waltham, MA, USA) online with a nano-ultra-high-pressure liquid chromatography system (Dionex, Ultimate 3000). Analysis was done in Label-Free Quantification mode and Data Dependent Acquisition (DDA). Raw files were then analyzed by Proteasome Discoverer (2.5), and proteins identified by Sequest-HT coupled with Percolator against a human UniProt database (UP000005640 − 9606, containing 82,685 entries). A contaminant list was included in the analysis. Carbamidomethylation of cysteine was set as static modification, whereas acetylation and ubiquitination were set as variable modification at lysine residues with phosphorylation ad serine or threonine residues. FDR was set at 0.01, and targets were validated using a concatenated target-decoy strategy. Proteins discussed in the results were filtered for the following parameters: (1) Identification with at least 2 peptides and 1 unique peptide; (2) identification in at least 50% of samples belonging to the same experimental group. The mass spectrometry proteomics data have been deposited to the ProteomeXchange Consortium via the PRIDE partner repository with the dataset identifier PXD054378 and https://doi.org/10.6019/PXD054378.

Statistical analysis

Statistical analyses were performed using the GraphPad Prism program.

Results

HDAC6 modulation influences the growth rate of cancer cells

Several cancer cell lines were treated at a range of ITF3756 from 250 nM to 5 µM. Cell growth was monitored over 72 h (Fig. S1A–D). At 48 h, crystal violet staining showed a marked reduction in HC1806 triple-negative breast cancer and B16F10 melanoma cell proliferation (Fig. S1E–F) at concentrations equal to or greater than 1 µM. HDAC6 inactivation by CRISPR-Cas9 in B16F10 cells confirmed the inhibitory effect of HDAC6 inhibition on cell proliferation. Figure S2A highlights a 20% growth decrease in HDAC6_KO cells compared to WT. Furthermore, the HDAC6-deprived cells exhibited a dampened and scattered growth pattern concerning WT cells and enhanced response to the 5 µM ITF3756 treatment (Fig. S2B).

HDAC6 modulation influences lysine acetylation dynamics

Remarkable changes in several acetylation markers were observed when HCC1806 cells were treated with 1 µM ITF3756 for 16 h. Immunofluorescence staining established a twofold to sixfold increase in the acetylation levels of H3K27, H3K9, and H3K14. In contrast, the levels of H4K16Ac decreased (Fig. 1A, B, Fig. S3A–B). These observations were validated by capillary electrophoresis analyses, which demonstrated an enrichment in the acetylation levels of H3K4Ac post-treatment. However, H3K23Ac was not modulated (as shown in Fig. S3C). This pattern of acetylation after ITF3756 treatment was consistent across other cell lines, including human and mouse triple-negative breast cancer cell lines MDA-MB-231 (Fig. S4A) and 4T1 (Fig. S4B), as well as the human leukemia T-lymphocyte Jurkat cell line (Fig. S4C). It is worth noting that the non-tumorigenic pulmonary Wi38 fibroblasts exhibited a different acetylation pattern (Fig. S4D). Different results emerged in the HDAC6_KO

(See figure on next page.)

Fig. 2 HDAC6 inhibition/inactivation increases α-Tubulin K40 acetylation. **A** Immunofluorescence analysis. Left: representative images showing the acetylation of α-Tubulin K40 (green signal) in the HCC1806 cell line. DAPI (blue signal) was used as a normalizer. Images were acquired at 20X magnification. Scale bar: 100 µm. Right: densitometric analysis of the mean fluorescent intensity (MFI). Error bars indicate SEM. Statistical analysis was performed by paired *t* test, $N = 3$; **$p < 0.005$. **B** Quantification of α-Tubulin K40 acetylation in HCC1806 cell line. Left: the panels show representative capillary electrophoresis experiments. The right graph represents the mean protein levels of α-Tubulin K40Ac, comparing the ITF3756-treated (green bar) to the vehicle-treated cells (black bar). The GAPDH was used as a normalizer. Error bars indicate SEM. Statistical analysis was performed by paired *t* test, $N = 3$; **$p < 0.005$. **C** Immunofluorescence staining: α-Tubulin K40Ac in B16F10 cells. Left: representative images showing the acetylation of α-Tubulin K40 (green signal) in the B16F10 cell line. DAPI (blue signal) was used as a normalizer. Images acquired at 20X magnification. Scale bar: 100 µm. Right: densitometric analysis of the mean fluorescent intensity (MFI). Error bars indicate SEM. Statistical analysis was performed by paired *t* test, $N = 3$; ***$p < 0.0005$. (**D**) Quantification of α-Tubulin K40 acetylation in B16F10 cells. Left: the panel shows a representative capillary electrophoresis experiment performed on the B16F10 cell line. The graph on the right represents the mean protein level of α-Tubulin K40Ac, comparing the KO_HDAC6 (green bar) and the WT (black bar) conditions. The β-Actin was used as a normalizer. Error bars indicate SEM. Statistical analysis was performed by paired *t* test, $N = 3$; ***$p < 0.0005$. **E** The graphs show the results of capillary electrophoresis experiments, detecting acetylation of α-Tubulin: K40 in HDAC6_KO mice (blue dots) compared to controls (WT, black dots) in liver, spleen, brain, and heart tissues. Error bars indicate SD. Statistical analysis was performed by unpaired *t* test, $N = 10$; ***$p < 0.0005$
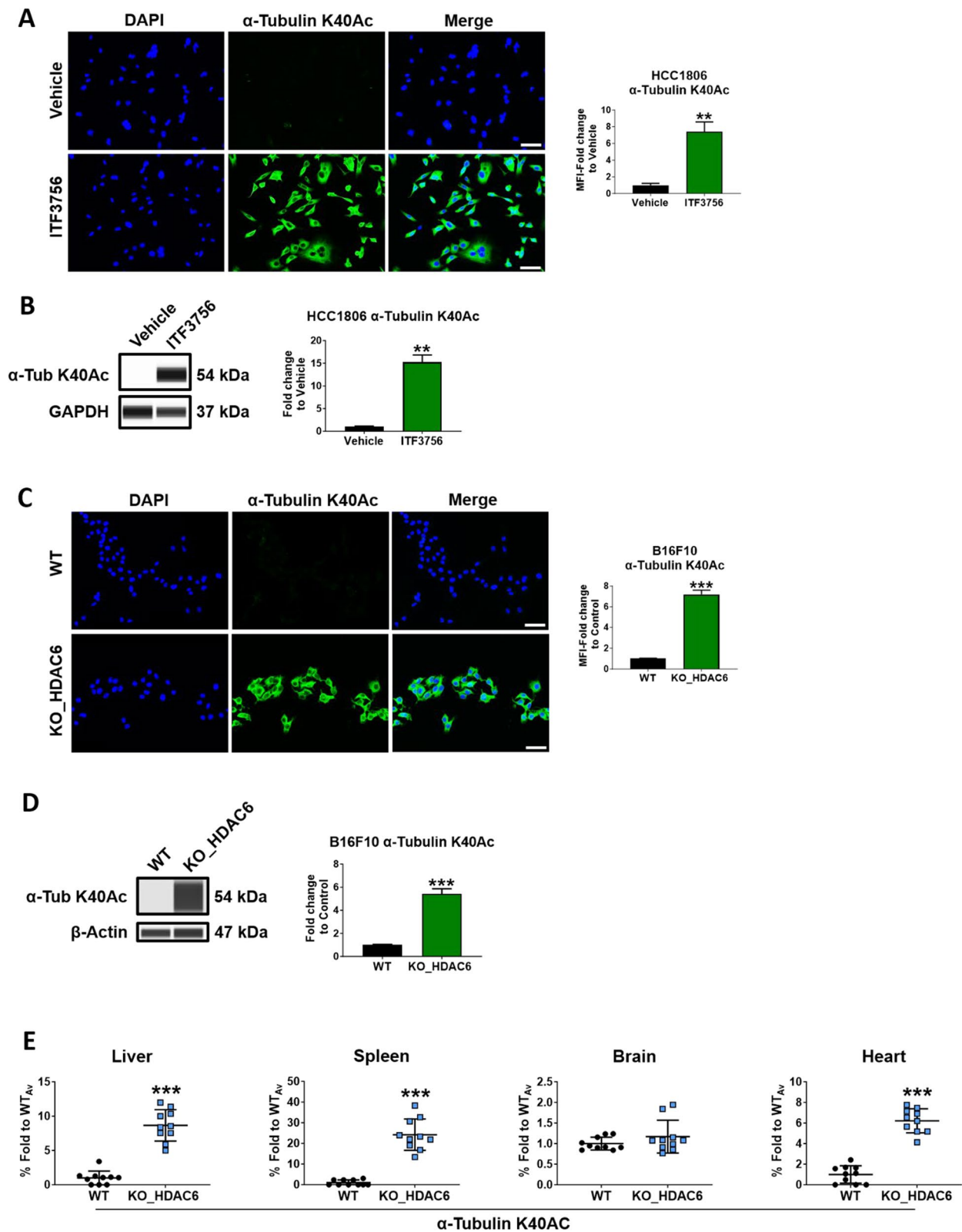
Fig. 2 (See legend on previous page.)

Zamperla *et al. Clinical Epigenetics*   (2024) 16:109

Page 8 of 20

cells. Immunofluorescence staining revealed a twofold enhancement in the acetylation levels of H3K27, H3K9, and H3K14 in the HDAC6-inactivated cells compared to their wild-type counterparts. Meanwhile, a decline in the H4K16Ac signal was recorded (Fig. 1C, D, Fig. S5A–B). These findings were supported by capillary electrophoresis analyses, which showed a similar enrichment in acetylation markers, including H3K4Ac, H3K9Ac, H3K14Ac, and H3K27Ac, while H3K23Ac and H4K16Ac remained relatively stable (Fig. S5C). When the B16F10 wild-type cells were exposed to 1 µM ITF3756 for 16 h, they mirrored the acetylation profiles observed in the HDAC6-inactivated cells, with significant increases, especially in H3K4Ac, H3K9Ac, H3K14Ac, and H3K27Ac histone markers (Fig. S5D). The effects of HDAC6 modulation are not limited to histone lysine modifications. They also extend to the acetylation of K40 on α-tubulin, a well-known target of HDAC6. Indeed, ITF3756 induced a pronounced increase in α-tubulin acetylation, as determined by immunofluorescence and capillary electrophoresis, in several cell lines (Fig. 2A, B and Fig. S4E, F). The same effect was observed in HDAC6_KO cells (Fig. 2C, D).

HDAC6 inactivation impacts lysine acetylation in vivo

We took advantage of HDAC6_KO mice to validate what was observed in vitro. Specific acetylation markers, including α-tubulin K40, H3K9, H3K14, H3K27, and H4K16, were investigated in both WT and HDAC6_KO mice by using capillary electrophoresis performed on tissue extracts from various organs, including liver, spleen,

brain, and heart. There was a significant increase in K40 acetylation in the liver (eightfold), spleen (25-fold), and heart samples (sixfold, Fig. 2E). However, the same result did not occur in the brain. In livers from HDAC6_KO mice, a slightly but significantly increased acetylation of H3 on lysine 9 and 27 was detected (Fig. 1E). Conversely, H3K14 and H4K16 did not change in HDAC6_KO animals. (Fig. S6A). In the spleen, acetylation of K27 on histone H3 was higher in HDAC6_KO mice (Fig. 1F), while H3K9, H3K14, and H4K16 did not change (Fig. 1F and S6B). Neither the brain nor the heart showed any considerable modification in histone acetylation levels (Fig. S6C-D).

HDAC6 inhibition/inactivation increases global HAT activity and shows elevated P300 protein levels

To delve deeper into the effects of ITF3756, we explored whether any changes were detectable in total HDAC and total HAT activities upon HDAC6 inhibition/inactivation. HCC1806 cells treated with ITF3756 1 µM for 16 h showed no alteration in total HDAC activity compared to the control (Fig. S7A, left panel). This result indicates that other HDACs might compensate for the loss of HDAC6 function or that a reduction in HDAC6 activity is insufficient to determine appreciable changes in global HDAC activity. However, there was a remarkable increase in global HAT activity in the ITF3756 conditions compared to the control solvent (Fig. 3A). Interestingly, global levels of acetyl-CoA (AcCoA), which serves as the substrate for HATs, remained unchanged (Fig. S7A,

(See figure on next page.)

Fig. 3 HDAC6 inhibition/inactivation increases total HAT activity and P300 protein level. **A** Total HAT activity assay was performed in the HCC1806 cell line, comparing ITF3756 1 µM 16 h treatment (green bar) and the control condition (black bar). Error bars indicate SEM. Data were analyzed by paired *t* test, $N=3$; **$p<0.005$. **B** P300 and HDAC6 protein expression. Left: representative image showing P300 and HDAC6 proteins in the HCC1806 cell line. Right: The graph reports the mean protein levels. Vinculin was used as a normalizer. Error bars indicate SEM. Multiple comparison two-way ANOVA was used to analyze the data, $N=5$; **$p<0.005$. **C** Immunofluorescence staining. Left: representative images showing P300 (green signal) and HDAC6-Flag (red signal) in the HCC1806 cell line after 24 h of pCDNA3_HDAC6_Flag transfection and 16 h treatment with 1 µM ITF3756. DAPI (blue signal) was used as a normalizer. Images were acquired at 20X magnification. Scale bar: 100 µm. Right: densitometric analysis of the mean fluorescent intensity (MFI). Error bars indicate SEM. Data were analyzed by paired *t* test, $N=3$; *$p<0.05$. **D** Protein expression analysis after HDAC6 silencing and P300 inhibitor EML425 treatment. Left: the panel indicates representative image of capillary electrophoresis experiments showing P300 and HDAC6 protein levels after HDAC6 silencing, quantifying P300, HDAC6, H3K9, and H3K27 acetylation on HCC1806 cell line after HDAC6 silencing and subsequent administration of 100 µM EML425 for 16 h. Right: the graph shows the mean protein signals of P300, HDAC6, H3K9Ac, and H3K27Ac in EML425-treated cells (orange bars) compared to vehicle-treated cells (gray bars). Scramble treated (red bars) and untreated cells (black bars) were used as controls. β-Actin and Vinculin were used as normalizers. Error bars indicate SEM. Statistical analysis was performed by multiple paired *t* tests, $N=3$; *$p<0.05$; **$p<0.005$. **E** Protein expression analysis after P300 silencing and HDAC6 inhibitor ITF3756 treatment, quantifying P300, HDAC6, H3K9, and H3K27 acetylation on HCC1806 cell line after P300 silencing and subsequent administration of 1 µM ITF3756 for 16 h. Left: representative capillary electrophoresis experiments. Right: the graph shows the mean protein signals of P300, HDAC6, H3K9Ac, and H3K27Ac in ITF3756-treated cells (blue bars) compared to vehicle-treated cells (gray bars). Scramble treated (green bars) and untreated cells (black bars) were used as controls. β-Actin and Vinculin were used as normalizers. Error bars indicate SEM. Statistical analysis was performed by multiple paired *t* tests, $N=3$; *$p<0.05$, **$p<0.005$. **F** Total HAT activity in the B16F10 cell line (HDAC6_KO, green bar, *vs* WT, black bar). Error bars indicate SEM. Data were analyzed by unpaired *t* test, $N=4$; ***$p<0.0005$. **G** Left: representative capillary electrophoresis experiment showing P300 and HDAC6 proteins in B16F10 cells. Right: mean protein levels of P300 and HDAC6. Vinculin was used as a normalizer. Error bars indicate SEM. Multiple comparison two-way ANOVA was used to analyze the data, $N=4$; *$p<0.05$; ***$p<0.0005$
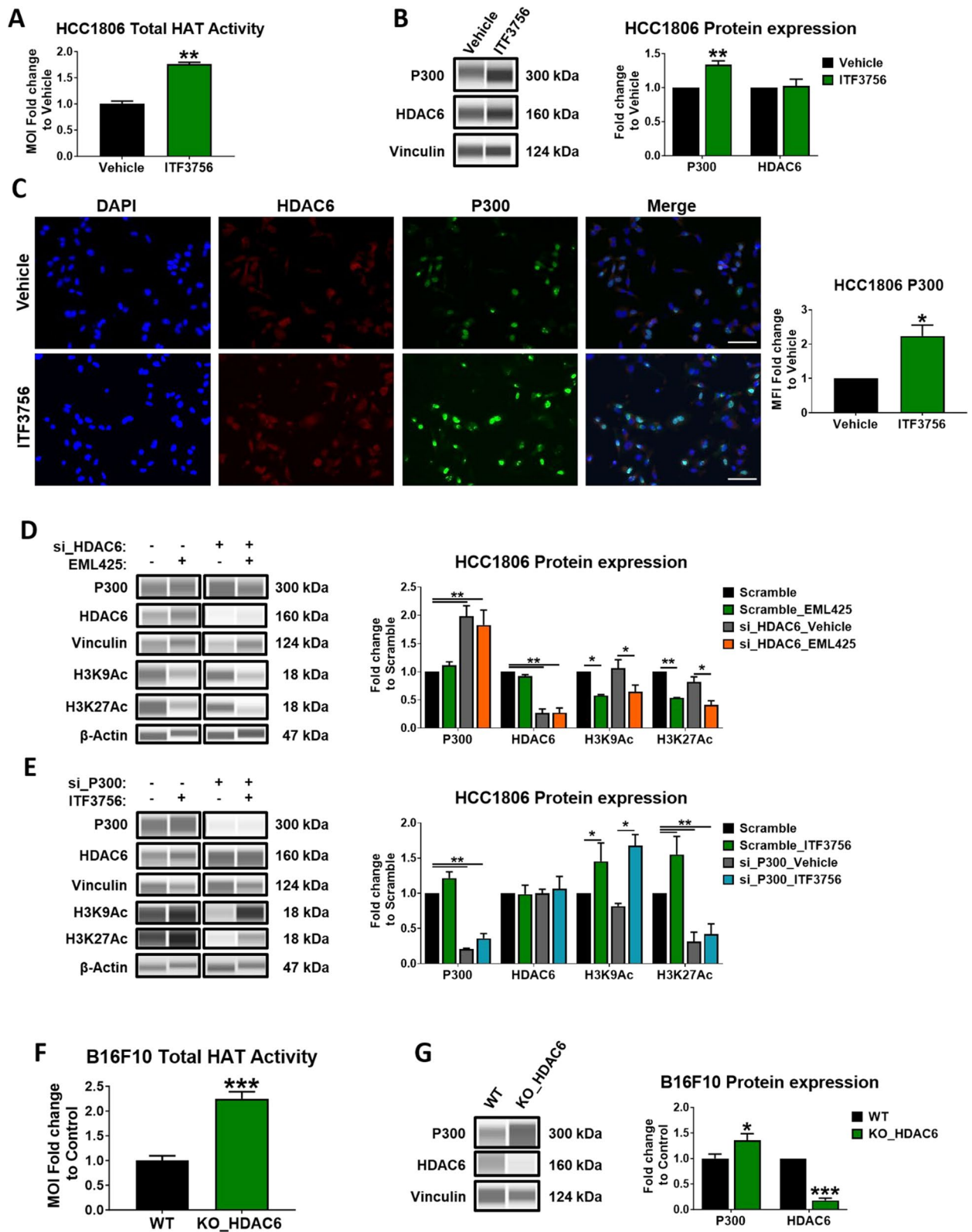
Zamperla *et al. Clinical Epigenetics*   (2024) 16:109

Page 9 of 20

Fig. 3 (See legend on previous page.)

Zamperla *et al. Clinical Epigenetics*   (2024) 16:109

Page 10 of 20

right panel), suggesting that the effect of HDAC6 inhibition on total HAT activity was not dependent on an altered metabolism of AcCoA. To get more insights, we evaluated whether P300, one of the most abundant HAT within cells and known to interact with HDAC6 [23], was affected by ITF3576 treatment. When we assessed the mRNA expression levels of HDAC6 and P300, we found no significant difference upon ITF3756 treatment (Fig. S7B), hinting that ITF3756 did not transcriptionally impact HDAC6 and P300 functions. However, capillary electrophoresis experiments showed increased P300 protein levels, as depicted in Fig. 3B, C, whereas HDAC6 protein levels were not modulated. A similar result was observed when HDAC6 was inactivated using siRNAs, leading to a decrease in HDAC6 expression by around 70% and a twofold increase of P300 protein levels (Fig. 3D). Of note, P300 inhibition by the small-molecule EML425 [32] led to a significant decrease in H3K9Ac and H3K27Ac levels in HCC1806 cells before and after HDAC6 inactivation by siRNAs (Fig. 3D).

Noteworthy, P300 inactivation, using siRNAs, did not change HDAC6 levels. In this condition, however, treating HCC1806 cells with ITF3756 1 µM for 16 h led to the accumulation of H3K9Ac, while H3K27Ac remained downregulated (Fig. 3E). Additionally, total HAT activity and P300 protein levels were notably higher in HDAC6_KO than in WT cells (Fig. 3F, G). Nevertheless, total HDAC activity, AcCoA levels, and P300 mRNA levels did not change (Fig. S7 C-D). Comparable results were obtained in ITF3756-treated Jurkat (Fig. S7E–F) and B16F10 cells (Fig. S7G–H).

HDAC6 inhibition promotes P300 stabilization

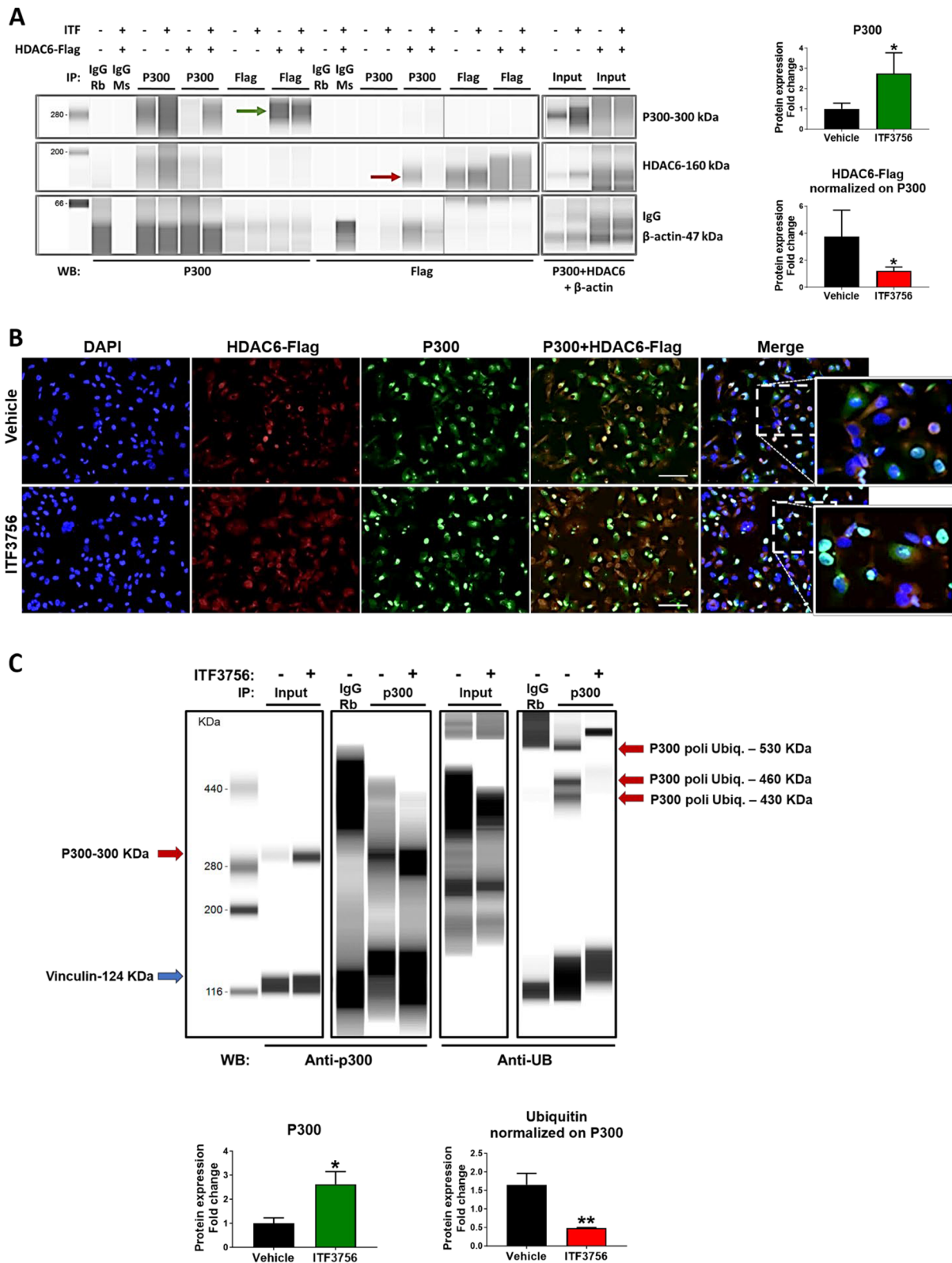HEK293T cells were transfected with pcDNA3.1+-HDAC6-Flag and control pcDNA3.1+(empty vector, EV). After 24 h, cells were exposed to 1 µM ITF3756 for an additional 16 h, and co-immunoprecipitation experiments, analyzed by capillary electrophoresis, were performed to assess whether a putative HDAC6/P300 complex could dissociate in the presence of ITF3576 (Fig. 4A). We found that in this cellular system, HDAC6-Flag content did not change after treatment, and the transfected protein was mainly localized in the cytoplasm in both conditions (Fig. 4 B). On the contrary, there was an evident increase in P300 levels in treated samples (Fig. 4A, B and Fig. S8). Furthermore, the enzyme appeared to be predominantly localized in the nucleus of ITF3576-treated cells than in controls. Moreover, we detected an HDAC6/P300 complex in untreated cells, significantly reduced after ITF3756 administration.

Proximity ligation assays (PLA) further confirmed these findings (Fig. S8). Indeed, in pcDNA3.1+-HDAC6-Flag-transfected MRC5 cells, a significant interaction was observed between the endogenous P300 and transfected HDAC6-Flag. This interaction was more pronounced than in the control cells expressing EV alone. Moreover, P300 levels increased upon ITF3576 treatment in pcDNA3.1+and pcDNA3.1+-HDAC6-Flag-transfected cells, as previously observed.

We then investigated which mechanism could support the increase in P300 protein levels detected upon ITF3576 treatment. Since P300 might undergo polyubiquitination and HDAC6 was reported to serve a role in Ub-signaling mechanisms, we evaluated whether HDAC6 inhibition could change the rate of P300 ubiquitination. To this aim, HCC1806 cells were exposed to 1 µM ITF3756 for 16 h, and immunoprecipitation with an anti-polyubiquitin antibody was performed (Fig. 4C). We observed a significant reduction in the polyubiquitinated species of P300 in the ITF3756-treated cells, compared to controls, despite the marked increase in P300 (Fig. 4C, bottom right).

(See figure on next page.)

Fig. 4 ITF3576 interferes with HDAC6/P300 association. **A** Left: Co-immunoprecipitation capillary electrophoresis experiments were performed on HEK293T cells transfected with pCDNA3.1+_HDAC6_Flag and pCDNA3.1+ as a control for 24 h and treated with 1 µM ITF3756 for an additional 16 h; DMSO was used as solvent control. The arrows indicate a decreased P300-HDAC6 interaction upon ITF3756 treatment. Right, top: mean protein levels of free P300 upon ITF3576 or vehicle treatment and immunoprecipitation with an anti-P300 antibody in pCDNA3.1+_HDAC6_Flag-transfected cells. Right, bottom: HDAC6-Flag protein levels upon ITF3576 or vehicle treatment and immunoprecipitation with an anti-P300 antibody in pCDNA3.1+_HDAC6_Flag-transfected cells-, normalized on respective P300 content. Error bars indicate SEM. Data were analyzed by unpaired *t* test, *N*=3; *p*<0.05. **B** Immunofluorescence. Representative images showing P300 (green signal) and HDAC6-Flag (red signal) in the HCC1806 cell line after 24 h of pcDNA3_HDAC6_Flag transfection and 16 h of treatment with 1 µM ITF3756. DAPI (blue signal) was used as a normalizer. Images were acquired at 20X magnification. Scale bar: 100 µm. **C** ITF3576 impairs P300 ubiquitination. Top: capillary electrophoresis experiments were performed on HCC1806 cells treated with 1 µM ITF3756 for 16 h compared to solvent control. Samples were immunoprecipitated with an anti-P300 antibody, blotted with an anti-P300 antibody (on the middle left), and an anti-polyubiquitin antibody (on the right). Arrows on the left indicate P300 (red) and the normalizer Vinculin (blue). The red arrows on the right show the P300 polyubiquitinated species. Bottom, left: P300 mean protein levels in ITF3756-treated cells (green bar) compared to solvent (black bar), measuring immunoprecipitated and blotted with anti-P300 antibody samples. Bottom, right: quantification of the mean content of the P300 ubiquitinated species, measuring samples immunoprecipitated with anti-P300 antibody and blotted with anti-polyubiquitin antibody, in cells treated with ITF3756 (red bar) compared to the control (black bar), and normalized on the respective P300 amount. Error bars indicate SEM. Data were analyzed by unpaired *t* test, *N*=3; *p*<0.05

Fig. 4 (See legend on previous page.)

Zamperla *et al. Clinical Epigenetics* (2024) 16:109

Page 12 of 20

To corroborate further the specificity of this observation and to rule out that P300 stabilization was not caused by global alterations of proteasome or Ub-signaling induced by ITF3756, canonical parameters of UPS activity were assayed in HCC1806 treated with 1 μM ITF3756 for 16 h and compared to controls (*i.e.*, solvent-treated).

Crude cell extracts (*i.e.*, the soluble fraction of cytosol) were isolated under non-denaturing conditions from ITF3756- and solvent-treated cells and assayed for the rate of cleavage of the fluorogenic probe LLVY-amc by the chymotrypsin-like activity of intact proteasome particles. The spectrofluorimetric assay is commonly called proteasome assay (see Methods). The slopes of each sample were then calculated over a linear interval. The data highlighted that the rate of cleavage of LLVY-amc (expressed as μmol/min) was fully comparable between ITF3756- and solvent-treated cells (Fig. S9A), suggesting that the drug did not alter the basal proteasome activity.

To strengthen this finding, the same extracts were further analyzed by WB. Filters were assayed for the overall content of (1) representative proteasome subunits, either belonging to the 20S (*i.e.*, PSMA7, PSMB6) and the 19S (*i.e.*, PSMD4); (2) Ub-proteins and those conjugated with Ub-K:48 linkages, which more truthfully identify proteasome substrates (*i.e.*, the K:48 topology of Ub-chains is the preferential configuration for substrate processing through the 26S proteasome; Fig. S9B, C).

Also, in this case, the data obtained after normalization suggested that the overall content in proteasome subunits and Ub-proteins was fully comparable between ITF3756- and solvent-treated cells.

Therefore, the overall data set suggests that ITF3756 treatment, reducing HDAC6/P300 association, might inhibit P300 ubiquitination through its stabilization.

HDAC6 inactivation affects chromatin accessibility

Transposase-accessible chromatin sequencing (ATAC-seq) assay and H3K27Ac chromatin immunoprecipitation sequencing (ChIP-seq) were performed on B16F10 HDAC6_KO and WT cell lines. Indeed, principal component analysis (PCA) shows that HDAC6_KO and WT cells are well separated in both analyses (Figs. 5–6A).

ATAC-seq and H3K27Ac-ChIP-seq experiments revealed a significant number of differentially accessible regions (DARs) with a $-0.5 \leq$ shrunken LogFC ≤ 0.5 and p-adjusted value ≤ 0.05 (Figs. 5–6B). Specifically, 4835 DARs were identified from the ATAC-seq and 9650 DARs from the ChIP-seq.

Regarding the genomic features, most different ATAC and H3K27Ac peaks between HDAC6_KO and WT samples occurred at introns and distal intergenic regions (Figs. 5–6C, red and green bars, respectively). The GO analysis revealed putative targets of HDAC6 inactivation (Figs. 5–6D). These analyses highlighted a different regulation of genes involved in cell proliferation (GO-ID: 0008283), cell adhesion (GO-ID: 0007155), and migration (GO-ID: 0016477), which were down-modulated due to inaccessible chromatin (Figs. 5–6D, upper panel, blue bars). Meanwhile, genes with a role in apoptotic pathways (GO-ID: 0043065) were upregulated due to increased chromatin accessibility (lower graph, red bars, in Figs. 5–6D). Specifically, by combining the HDAC6-associated DARs, identified by ATAC-seq and ChIP-seq analyses, two protein networks related to down- and upregulated regions, respectively, were generated, pointing out a series of genes associated with an altered survival program including *Akt1, Itgb3, Gas6, Sox9, Nf1, Tgfb2,* and *Casp7* (Fig. 7A, B).

Similar results were obtained by analyzing Jurkat cells treated with 1 μM ITF3756 for 16 h compared to solvent controls by ATAC-seq and H3K27ac-ChIP-seq. The PCA showed that the two samples were well separated (Figs. S10–S11A); the ATAC-seq revealed 1399 DARs and the ChIP-seq 11,450 DARs with a $-0.5 \leq$ shrunken LogFC ≤ 0.5 and p-adjusted value ≤ 0.05 (Figs. S10–S11B). Again, the most affected genomic features were the introns and the distal intergenic regions (Figs. S10–S11C, red and green bars, respectively). Once more, the GO analyses showed a different regulation in the biological processes related to cell proliferation, cell adhesion, and apoptosis (Figs. S10–S11D).

(See figure on next page.)

Fig. 5 Chromatin accessibility landscape of KO_HDAC6 *vs.* WT B16F10 cells revealed by ATAC-Seq. A The principal component analysis results on the whole dataset in KO_HDAC6 B16F10 cells (green dots) compared to WT control (black dots). $N = 3$. **B** Volcano plot of differentially accessible regions. The accessible regions are toward the right, the inaccessible are toward the left, and the most statistically significant are toward the top. Red dots represent significant open and closed regions with $-0.5 \leq$ shrunken LogFC ≤ 0.5 and a *p*-adjusted value ≤ 0.05. Black dots represent non-significant changes. $N = 3$. **C** The graph illustrates the distribution of the differentially accessible regions of specific genomic features depicted as follows: distal intergenic regions (green), downstream regions (yellow) encompassing 3000 bp from transcription end site (TES), introns (red), coding exons (orange), 3′ UTRs (light blue) and 5′ UTRs (pink), proximal (0–1000 bp, blue), and distal promoter (violet) encompassing 3000 bp upstream of the transcription start site (TSS). **D** Gene ontology analysis of differentially accessible regions between KO_HDAC6 and WT cells: inaccessible regions (ICR, blue bar graph, upper panel) and accessible chromatin regions (ACR, red bar graph, lower panel). $N = 3$
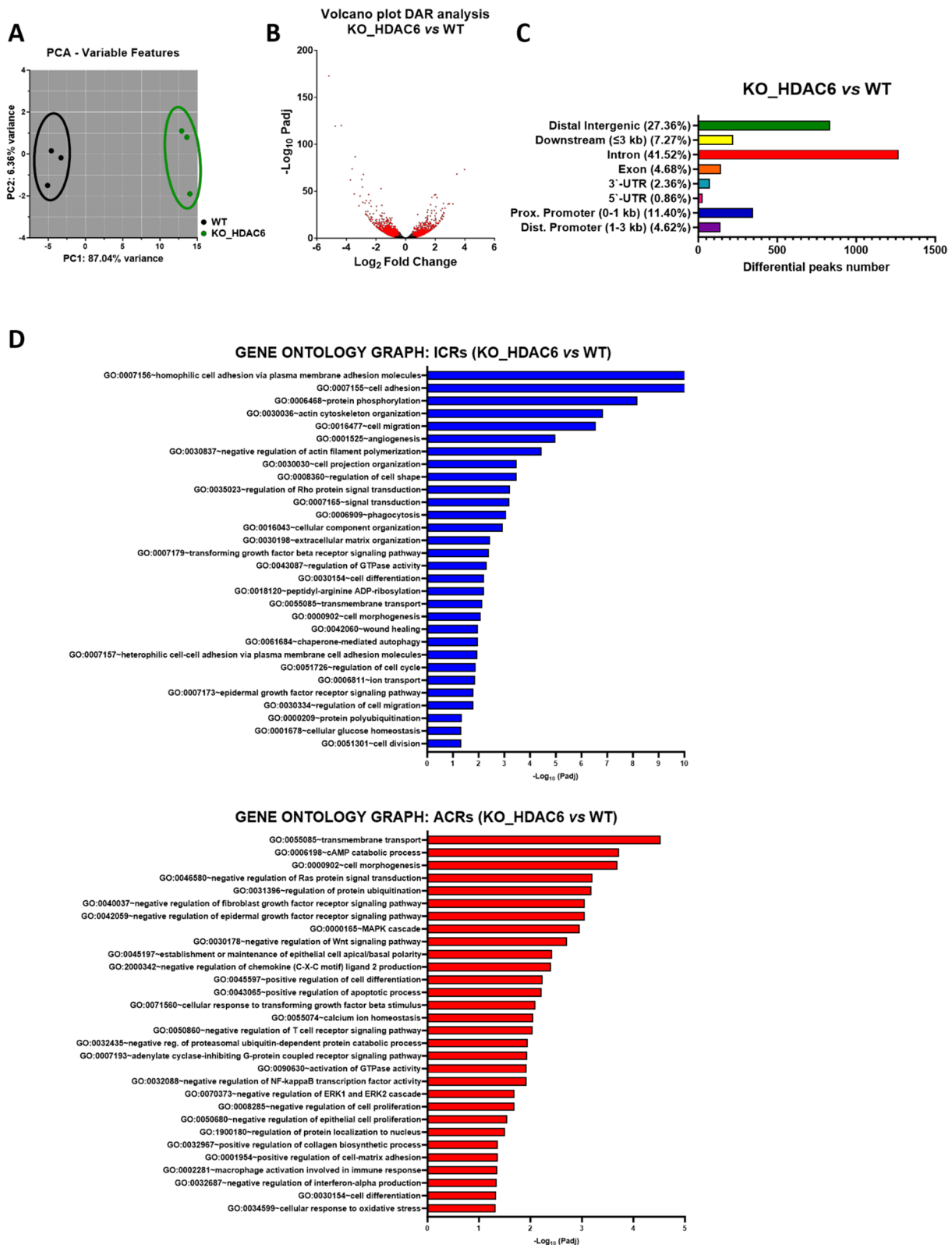
Fig. 5 (See legend on previous page.)

Zamperla *et al. Clinical Epigenetics*   (2024) 16:109

Page 14 of 20

The effect of HDAC6 inactivation in B16F10 cells has been further assessed by comparing the KO_HDAC6 and the WT condition by transcriptome analysis. Genes with $-1 \leq \mathrm{Log2FC} \leq 1$ and p-adjusted value ≤ 0.1 were considered differentially expressed (DE) and retained for further analysis. Through DESeq2 analysis, it was possible to identify 554 up- and 778 downregulated genes in the KO_HDAC6 condition. The PCA analysis distinguishes the two conditions (Fig. S12A). The volcano plot highlighted all statistically significant DE genes in the two subgroups; the expression difference is considered significant for a $-1 \leq \mathrm{Log2FC} \leq 1$ and p-adjusted value ≤ 0.1. Red dots represent significantly up- and downregulated genes with $1 \leq \mathrm{Log2FC} \leq 1$ (*x*-axis) and a p-adjusted value ≤ 0.1 (*y*-axis; Fig. S12B). The 60 most modulated genes were selected and represented in the heatmap, in which the cluster genes, separated according to their degree of modulation, could be observed. KO_HDAC6 samples appeared to have gene expression profiles different from WT controls (Fig. S12C). To further explore the mechanisms underlying the differences observed between the two groups, GO term enrichment analysis for DE genes DE_KO_HDAC6_*vs*_WT was performed for both upregulated and downregulated genes. In the dot-plot graph, results are represented according to the criterion for which the red dots are the most significantly differentially regulated; while the point size indicates the number of genes involved in the process, the dot position represents the expression fold change. The biological processes, the cell components, the molecular functions, and the KEGG pathways analyses of KO_HDAC6 samples revealed a significant modulation in genes correlated with the extracellular matrix, cell adhesion, cell motility, regulation of protein stability, channel activity, signal transduction, and receptor complexes (Fig. S12D–G).

Of note, the change in the expression of some of the genes associated with an altered survival program (*Casp7, Sox9, Smad 3, Itgb3, Nf1,* and *Tgfb2*) was validated by RT-qPCR (Fig. 7C).

Furthermore, proteomic analyses were performed on HCC1806 scramble and HDAC6-silenced cells. Among the 3010 proteins identified (Fig. S13A, B), the gene ontology analysis of upregulated or downregulated proteins between HDAC6-silenced and scrambled cells revealed a significant modulation (Log2FC = 0.58 and *p*-adjusted value ≤ 0.05, Benjamini–Hochberg correction). Specifically, also in this condition, from the GO analysis, we observed modulation in proteins related to the process of cell proliferation (GO-ID:0008283), cell adhesion (*e.g.,* GO-ID: 0007155), cell migration (GO-ID: 0016477), extracellular matrix organization (GO-ID: 0030198), channel activity and integrin binding (*e.g.,* GO-ID: 0005178, Fig. S13C–H) confirming the data provided by the transcriptomic analyses on HDAC6_KO B16F10 cells.

Discussion

The dynamic balance between histone acetyltransferases (HATs) and histone deacetylases (HDACs) is essential for regulating acetylation levels within the cell. Acetylation and deacetylation of histones and other proteins influence cellular processes, chromatin structure, and gene expression. HDAC inhibitors shift this balance toward increased acetylation, potentially leading to a more open chromatin state and altered gene expression. Accordingly, the therapeutic benefits of HDAC inhibitors may be partly due to their broader effects on the cellular acetylation landscape, a process influenced by the interplay between HDACs and HATs [33].

Evidence suggests that HDAC pan-inhibitors can stabilize P300 [34]. HDAC inhibitors promote HAT autoacetylation and enhance P300 activity, leading to increased acetylation of histones and other proteins and ultimately influencing gene expression. Autoacetylation can also affect P300's interactions and stability, crucial in cellular processes and diseases [35]. Trichostatin A, a well-known HDAC pan-inhibitor, promotes P300 stabilization and lysine acetylation on several substrates, including transcription factors, signaling proteins, and histones [34, 36]. This effect might be linked to P300 autoacetylation and its interactions with specific targets, such as retinoic

(See figure on next page.)

Fig. 6 Chromatin accessibility landscape of KO_HDAC6 *vs* WT B16F10 cells revealed by H3K27Ac-ChIP-seq. **A** The principal component analysis results on the whole dataset in KO_HDAC6 B16F10 cells (green dots) compared to WT control (black dots). *N* = 3. **B** Volcano plot of differentially accessible regions. The H3K27Ac enriched regions are toward the right, the H3K27Ac decreased regions are toward the left, and the most statistically significant are toward the top. Red dots represent significant H3K27Ac enriched and decreased regions with $-0.5 \leq$ shrunken LogFC ≤ 0.5 and a *p*-adjusted value ≤ 0.05. Black dots represent non-significant changes. *N* = 3. **C** The graph illustrates the distribution of the differentially accessible regions of specific genomic features depicted as follows: distal intergenic regions (green), downstream regions (yellow) encompassing 3000 bp from transcription end site (TES), introns (red), coding exons (orange), 3′ UTRs (light blue) and 5′ UTRs (pink), proximal (0–1000 bp, blue), and distal promoter (violet) encompassing 3000 bp upstream of the transcription start site (TSS). **D** Gene ontology analysis of differentially accessible regions between KO_HDAC6 and WT cells revealed by H3K27Ac-ChIP-seq: inaccessible regions (ICR, blue bar graph, upper panel) and accessible chromatin regions (ACR, red bar graph, lower panel). *N* = 3
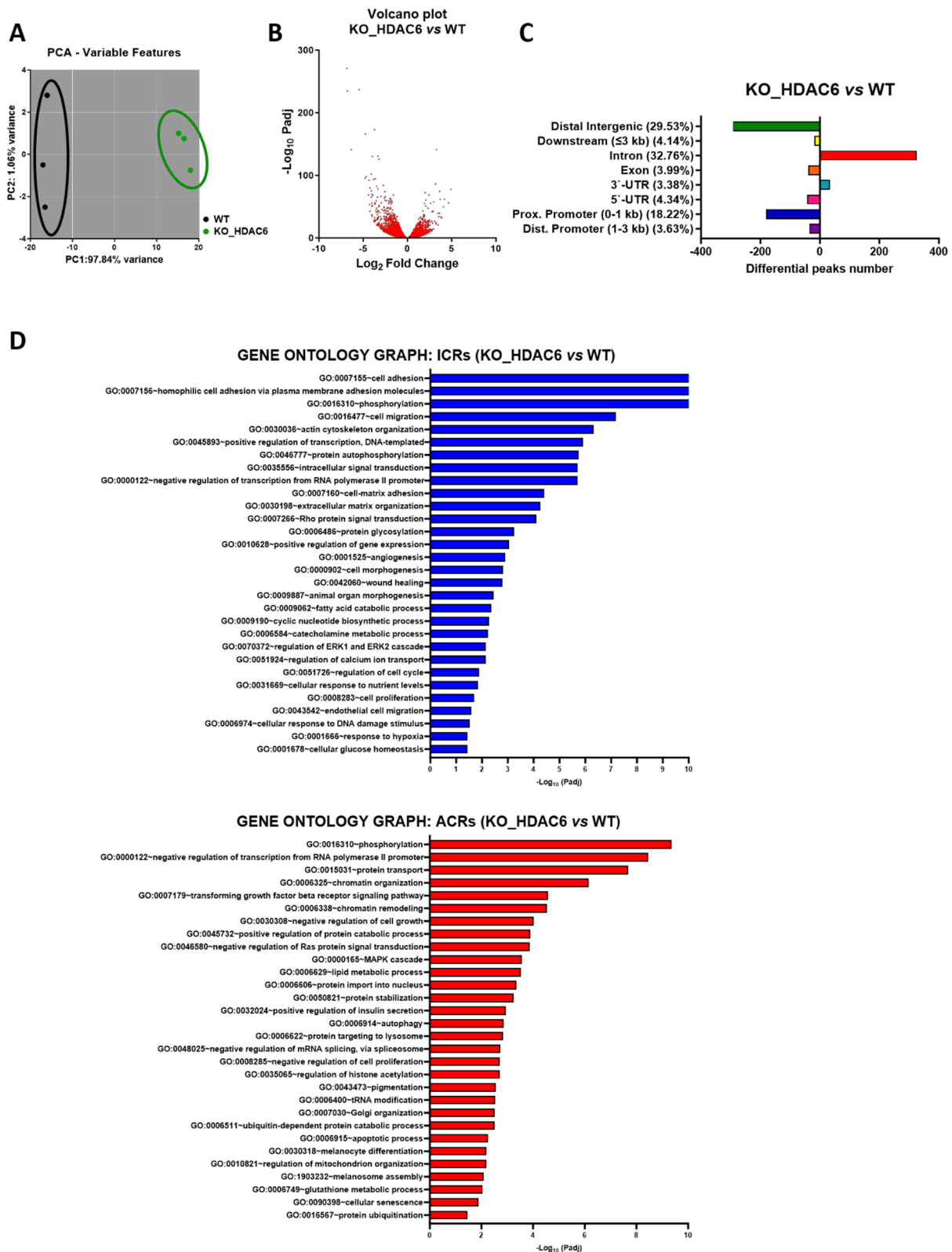
Fig. 6 (See legend on previous page.)

Zamperla *et al. Clinical Epigenetics*   (2024) 16:109

Page 16 of 20

acid receptor alpha or HIPK2 kinase [37]. However, the specific role of HDAC6 in this context remains to be thoroughly investigated.

Nevertheless, emerging evidence suggests that HDAC6 may also interact with other HDAC family members, potentially influencing their activity and function and impacting transcriptional regulation and cellular processes. Along with HDAC1 and HDAC2, HDAC6 is part of the chromatin remodeling complexes enriched in active genes, supporting their collaborative roles in gene regulation [38]. Besides, the complex formation between HDAC6 and HDAC1 or HDAC3 may modulate transcriptional repression, alter the deacetylation of specific substrates, or affect various cellular processes such as cell cycle progression and stress responses [39].

SIRT2, a class III HDAC family member, has been linked to the deacetylation of P300. Inhibitors of sirtuins can increase HAT activity and promote P300 stability. While HDAC6 interacts with SIRT2, evidence suggests it does not directly regulate P300 acetylation and stability [40, 41]. Conversely, the interaction between P300 and HDAC6 appears to negatively regulate the deacetylase activity of HDAC6 [23, 24].

The ITF3756 inhibitor demonstrates a selective affinity for HDAC6 at nanomolar or low micromolar concentrations [29]. It is well tolerated in cells from various primary tumor types. Under these experimental conditions, we observed minimal changes in overall HDAC activity, suggesting that ITF3756 does not significantly affect the most active HDACs, including class I enzymes. Notably, we found a marked increase in histone H3 lysine acetylation across all tested conditions, especially at Lysine 9, 14, and 27 residues, of which, as expected, lysine 27 seemed the most sensitive to the P300 acetylation function.

Our experiments revealed that a complex between HDAC6 and P300 in the cytoplasm dissociates upon treatment with ITF3756. The specific mechanism behind this dissociation remains unclear, but it could be due to changes in the HDAC6 protein structure caused by the inhibitor binding [37]. Similar effects have been observed for other protein complexes with different HDAC inhibitors, including those targeting HDAC6 specifically, such as Tubacin. These inhibitors disrupt HDAC6 protein complexes, leading to functional consequences. For example, dissociation of HDAC6 from PP1 phosphatase by an HDAC inhibitor resulted in increased PP1 activity [40]. The effect of ITF3756 on HDAC6 and P300 coincides with a significant increase in histone H3 lysine acetylation observed across all experimental conditions, including cells treated with ITF3756, those transfected with HDAC6-silencing siRNA, and those with genetically inactivated HDAC6.

Interestingly, we observed increased levels of acetylated histone H3 in liver and spleen tissue from HDAC6 knock-out mice, while levels remained unchanged in heart and brain tissue. The reason for this tissue-specific difference is currently unclear. However, a potential explanation could be the difference in proliferative capacity between these organs. The liver and spleen can regenerate in response to injury or infection, whereas the heart and brain have limited regenerative potential. This observation aligns with findings in DNA methylation, where heart and brain tissues show higher levels of methylated cytosine than organs with greater proliferative capacity [42, 43]. Bioinformatic analyses provided a deeper understanding of the changes caused by HDAC6 inactivation. These analyses focused on how HDAC6 loss affects gene expression patterns and chromatin accessibility, offering valuable insights into the molecular processes occurring within cancer cells [44]. Gene Ontology (GO) analysis was particularly helpful in identifying changes in gene regulation, especially in genes involved in cell proliferation, adhesion, and migration. The downregulation of genes in these categories suggests a potential mechanism by which HDAC6 inactivation can counteract cancer cell growth and metastasis [45]. This reduced accessibility may reflect a more condensed chromatin state, making it harder for the transcriptional machinery to access important oncogenic regions [46].

Another significant finding was the upregulation of genes involved in apoptosis upon HDAC6 inactivation. This observation suggests that chromatin becomes more relaxed in regions controlling these apoptotic processes, potentially allowing for increased gene transcription that drives cell death. This shift toward apoptosis is intriguing as it suggests a potential therapeutic target: promoting cell death in cancer cells [47]. Further insights into these epigenetic changes were gained by combining ATAC-seq

(See figure on next page.)

Fig. 7 ATAC-seq and H3K27Ac-ChIP-seq integrated analysis in KO_HDAC6 *vs* WT B16F10 cells. **A** Venn diagram (left) and gene network analysis (right) show the intersection between downregulated genes identified by ATAC-seq and H3K27Ac-ChIP-seq analysis associated with cell proliferation, cell adhesion, and apoptosis. **B** Venn diagram (left) and gene network analysis (right) show the intersection between upregulated genes identified by ATAC-seq and H3K27Ac-ChIP-seq analysis associated with cell proliferation, cell adhesion, and apoptosis. **C** GO target validation: mRNA levels assayed by RT-qPCR in B16F10 HDAC6_KO (green bars) *vs* WT (black bars). Gapdh was used as a normalizer, and relative mRNA expression was calculated using the $2^{-\Delta\Delta Ct}$ method. Error bars indicate SEM. Multiple *t* tests, $N = 5$, performed statistical analysis; ***$p < 0.0005$
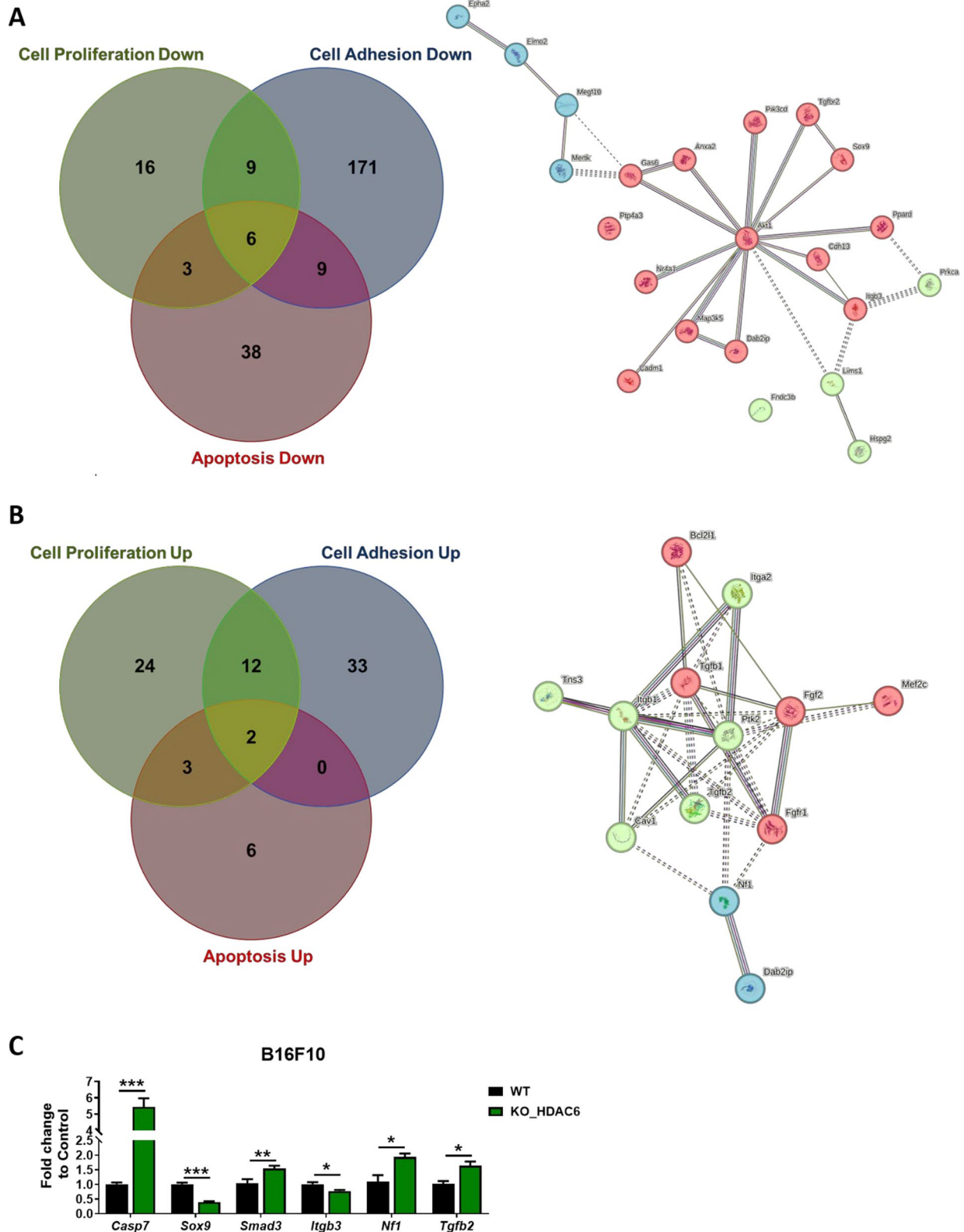
Fig. 7 (See legend on previous page.)

Zamperla *et al. Clinical Epigenetics*   (2024) 16:109

Page 18 of 20

and ChIP-seq analyses. These techniques identified specific genes for cell survival programs, such as Akt1, Itgb3, Gas6, Sox9, Nf1, Tgfb2, and Casp7. Each of these genes plays a critical role in cellular processes, and their altered expression due to HDAC6 loss could significantly impact cancer cell survival, proliferation, and ability to spread. For example, the downregulation of Akt1, a key signaling molecule involved in cell cycle and survival, could directly reduce the viability and aggressiveness of cancer cells. Similarly, the downregulation of Sox9, a transcription factor critical for cell fate and tumor formation, could affect cancer cell differentiation and invasive potential [48].

These findings highlight the epigenomic effects of HDAC6 inactivation and suggest potential biomarkers to predict the response to HDAC6 inhibitor therapy. Interestingly, our observation resembles HDAC8 inactivation, determining a significant increase in acetylated lysine 27 [49]. Nevertheless, HDAC8 contributes to tubulin deacetylation in specific conditions, similar to HDAC6 [50].

Monitoring the expression levels of the identified genes might help assess the effectiveness of HDAC6-targeted treatments and could guide personalized treatment decisions based on a patient's specific tumor profile. Additionally, the differential regulation of these genes indicates the potential for synergistic effects when combining HDAC6 inhibitors with other targeted therapies. For example, combining HDAC6 inhibition with drugs that target the AKT pathway could offer enhanced antitumor effects in cancers where this pathway is abnormally active [51, 52].

Our work reveals a broader perspective on HDAC6's role in the epigenetic regulation of cancer cells. This role includes HDAC6's direct deacetylation function and its broader effects on chromatin structure, ultimately influencing gene expression. Notably, the changes in the epigenetic landscape caused by HDAC6 cannot be separated clearly from the function of P300. HDAC6 inhibition stabilizes this crucial acetylase, increasing lysine acetylation (such as enrichment of H3K27Ac) and contributing to the observed chromatin remodeling [53–55]. This aspect of HDAC6 function is particularly relevant given the growing interest in multi-targeted epigenetic therapies for cancer treatment [56]. In this light, the bioinformatic analyses in this study offer valuable insights into the molecular changes caused by HDAC6 inactivation, broadening our understanding of the complex relationship between epigenetic regulation and cancer cell behavior, further suggesting HDAC6 as a promising therapeutic target for various cancers [57].

This study highlights the potential of the ITF3736 inhibitor for epigenetic modulation in cancer. By disrupting the HDAC6-P300 interaction, ITF3736 stabilizes P300, leading to increased overall HAT activity and histone acetylation. This effect is further supported by the observed decrease in P300 ubiquitination, indicating enhanced protein stability and function. Additionally, histone H3 lysine acetylation enrichment, particularly at lysine 27, suggests broad chromatin remodeling resulting from the HDAC6-P300 dissociation. Targeting this interaction can pave the way for novel cancer therapies to restore normal epigenetic control of chromatin structure and protein function.

Supplementary Information

The online version contains supplementary material available at https://doi.org/10.1186/s13148-024-01725-8.

> Additional file1 (DOCX 11960 kb)

Availability of data and materials
All data are available in the main text or the supporting information. Next-generation sequencing (NGS) data generated from ATAC-seq and ChIP-seq have been deposited in GEO under accession numbers GSE273644 and GSE273645. RNA-seq data generated via Illumina are available online at http://support.illumina.com/downloads/bcl-2fastq-conversion-software-v217.html. KEGG pathway analysis is available online at https://www.genome.jp/kegg/pathway.html. Proteomics data are available via ProteomeXchange with identifier PXD054378. Any additional information is available from the corresponding author upon request.

Declarations

Ethics approval and consent to participate
N/A.

Consent for publication
All authors agreed to this publication.

Competing interest
CP, GF, and CS are employed by Italfarmaco SpA, the owner of the ITF3756 commercial rights.

Author details
[1]Laboratory of Epigenetics, Istituti Clinici Scientifici Maugeri IRCCS, 27100 Pavia, Italy. [2]Institute of Molecular Biology and Pathology, National Research Council (CNR), c/o Sapienza University of Rome, 00185 Rome, Italy.

Zamperla *et al. Clinical Epigenetics*   (2024) 16:109

Page 19 of 20

[3]Institute for Systems Analysis and Computer Science, National Research Council (CNR)-IASI, 00185 Rome, Italy. [4]Molecular Biology and Transcriptomics Unit, IRCCS Mondino Foundation, 27100 Pavia, Italy. [5]IRCCS-Fondazione Bietti, Rome, Italy. [6]Institute of Molecular Genetics, National Research Council (CNR), 27100 Pavia, Italy. [7]New Drug Incubator Department, Italfarmaco Group, 20092 Cinisello Balsamo, Italy.

References

1. Milazzo G, Mercatelli D, Di Muzio G, Triboli L, De Rosa P, Perini G, et al. Histone deacetylases (HDACs): evolution, specificity, role in transcriptional complexes, and pharmacological actionability. Genes (Basel). 2020;11(5):556.

2. Hubbert C, Guardiola A, Shao R, Kawaguchi Y, Ito A, Nixon A, et al. HDAC6 is a microtubule-associated deacetylase. Nature. 2002;417(6887):455–8.

3. Zhang X, Yuan Z, Zhang Y, Yong S, Salas-Burgos A, Koomen J, et al. HDAC6 modulates cell motility by altering the acetylation level of cortactin. Mol Cell. 2007;27(2):197–213.

4. Lin YH, Major JL, Liebner T, Hourani Z, Travers JG, Wennersten SA, et al. HDAC6 modulates myofibril stiffness and diastolic function of the heart. J Clin Invest. 2022;132:10.

5. Kovacs JJ, Murphy PJ, Gaillard S, Zhao X, Wu JT, Nicchitta CV, et al. HDAC6 regulates Hsp90 acetylation and chaperone-dependent activation of glucocorticoid receptor. Mol Cell. 2005;18(5):601–7.

6. Fusco C, Micale L, Augello B, Mandriani B, Pellico MT, De Nittis P, et al. HDAC6 mediates the acetylation of TRIM50. Cell Signal. 2014;26(2):363–9.

7. Li L, Yang XJ. Tubulin acetylation: responsible enzymes, biological functions and human diseases. Cell Mol Life Sci. 2015;72(22):4237–55.

8. Li Y, Shin D, Kwon SH. Histone deacetylase 6 plays a role as a distinct regulator of diverse cellular processes. FEBS J. 2013;280(3):775–93.

9. Yang Y, Rao R, Shen J, Tang Y, Fiskus W, Nechtman J, et al. Role of acetylation and extracellular location of heat shock protein 90alpha in tumor cell invasion. Cancer Res. 2008;68(12):4833–42.

10. Sadoul K, Boyault C, Pabion M, Khochbin S. Regulation of protein turnover by acetyltransferases and deacetylases. Biochimie. 2008;90(2):306–12.

11. Xu Y, Wan W. Acetylation in the regulation of autophagy. Autophagy. 2023;19(2):379–87.

12. Valenzuela-Fernandez A, Cabrero JR, Serrador JM, Sanchez-Madrid F. HDAC6: a key regulator of cytoskeleton, cell migration and cell-cell interactions. Trends Cell Biol. 2008;18(6):291–7.

13. Tsujimoto K, Jo T, Nagira D, Konaka H, Park JH, Yoshimura SI, et al. The lysosomal ragulator complex activates NLRP3 inflammasome in vivo via HDAC6. EMBO J. 2023;42(1): e111389.

14. Kulthinee S, Yano N, Zhuang S, Wang L, Zhao TC. Critical Functions of histone deacetylases (HDACs) in modulating inflammation associated with cardiovascular diseases. Pathophysiology. 2022;29(3):471–85.

15. Seidel C, Schnekenburger M, Dicato M, Diederich M. Histone deacetylase 6 in health and disease. Epigenomics. 2015;7(1):103–18.

16. Chen J, Li Q. Life and death of transcriptional co-activator p300. Epigenetics. 2011;6(8):957–61.

17. Ghosh AK. Acetyltransferase p300 Is a putative epidrug target for amelioration of cellular aging-related cardiovascular disease. Cells. 2021;10:11.

18. Sun H, Yang X, Zhu J, Lv T, Chen Y, Chen G, et al. Inhibition of p300-HAT results in a reduced histone acetylation and down-regulation of gene expression in cardiac myocytes. Life Sci. 2010;87(23–26):707–14.

19. Lu P, Xu Y, Sheng ZY, Peng XG, Zhang JJ, Wu QH, et al. De-ubiquitination of p300 by USP12 critically enhances METTL3 expression and Ang II-induced cardiac hypertrophy. Exp Cell Res. 2021;406(1): 112761.

20. Girdwood D, Bumpass D, Vaughan OA, Thain A, Anderson LA, Snowden AW, et al. P300 transcriptional repression is mediated by SUMO modification. Mol Cell. 2003;11(4):1043–54.

21. Sankar N, Baluchamy S, Kadeppagari RK, Singhal G, Weitzman S, Thimmapaya B. p300 provides a corepressor function by cooperating with YY1 and HDAC3 to repress c-Myc. Oncogene. 2008;27(43):5717–28.

22. Bobrowska A, Paganetti P, Matthias P, Bates GP. Hdac6 knock-out increases tubulin acetylation but does not modify disease progression in the R6/2 mouse model of Huntington's disease. PLoS ONE. 2011;6(6): e20696.

23. Han Y, Jeong HM, Jin YH, Kim YJ, Jeong HG, Yeo CY, et al. Acetylation of histone deacetylase 6 by p300 attenuates its deacetylase activity. Biochem Biophys Res Commun. 2009;383(1):88–92.

24. Liu Y, Peng L, Seto E, Huang S, Qiu Y. Modulation of histone deacetylase 6 (HDAC6) nuclear import and tubulin deacetylase activity through acetylation. J Biol Chem. 2012;287(34):29168–74.

25. Getsy PM, Coffee GA, Kelley TJ, Lewis SJ. Male histone deacetylase 6 (HDAC6) knock-out mice have enhanced ventilatory responses to hypoxic challenge. Res Sq. 2023;14:1332810.

26. Dallavalle S, Pisano C, Zunino F. Development and therapeutic impact of HDAC6-selective inhibitors. Biochem Pharmacol. 2012;84(6):756–65.

27. Zhao Y, Liang T, Hou X, Fang H. Recent development of novel HDAC6 isoform-selective inhibitors. Curr Med Chem. 2021;28(21):4133–51.

28. Ripamonti C, Spadotto V, Pozzi P, Stevenazzi A, Vergani B, Marchini M, et al. HDAC inhibition as potential therapeutic strategy to restore the deregulated immune response in severe COVID-19. Front Immunol. 2022;13: 841716.

29. Vergani B, Sandrone G, Marchini M, Ripamonti C, Cellupica E, Galbiati E, et al. Novel benzohydroxamate-based potent and selective histone deacetylase 6 (HDAC6) inhibitors bearing a pentaheterocyclic scaffold: design, synthesis, and biological evaluation. J Med Chem. 2019;62(23):10711–39.

30. Elsasser S, Schmidt M, Finley D. Characterization of the proteasome using native gel electrophoresis. Methods Enzymol. 2005;398:353–63.

31. Sbardella D, Tundo GR, Coletta M, Manni G, Oddone F. Dexamethasone downregulates autophagy through accelerated turnover of the Ulk-1 complex in a trabecular meshwork cells strain: insights on steroid-induced glaucoma pathogenesis. Int J Mol Sci. 2021;22(11):5891.

32. Milite C, Feoli A, Sasaki K, La Pietra V, Balzano AL, Marinelli L, et al. A novel cell-permeable, selective, and noncompetitive inhibitor of KAT3 histone acetyltransferases from a combined molecular pruning/classical isosterism approach. J Med Chem. 2015;58(6):2779–98.

33. Slaughter MJ, Shanle EK, Khan A, Chua KF, Hong T, Boxer LD, et al. HDAC inhibition results in widespread alteration of the histone acetylation landscape and BRD4 targeting to gene bodies. Cell Rep. 2021;34(3): 108638.

34. Kim SH, Kang HJ, Na H, Lee MO. Trichostatin A enhances acetylation as well as protein stability of ERalpha through induction of p300 protein. Breast Cancer Res. 2010;12(2):R22.

35. Jain S, Wei J, Mitrani LR, Bishopric NH. Auto-acetylation stabilizes p300 in cardiac myocytes during acute oxidative stress, promoting STAT3 accumulation and cell survival. Breast Cancer Res Treat. 2012;135(1):103–14.

36. Ryan CM, Harries JC, Kindle KB, Collins HM, Heery DM. Functional interaction of CREB binding protein (CBP) with nuclear transport proteins and modulation by HDAC inhibitors. Cell Cycle. 2006;5(18):2146–52.

37. Choi JR, Lee SY, Shin KS, Choi CY, Kang SJ. p300-mediated acetylation increased the protein stability of HIPK2 and enhanced its tumor suppressor function. Sci Rep. 2017;7(1):16136.

38. Delcuve GP, Khan DH, Davie JR. Roles of histone deacetylases in epigenetic regulation: emerging paradigms from studies with inhibitors. Clin Epigenetics. 2012;4(1):5.

39. Wang P, Wang Z, Liu J. Role of HDACs in normal and malignant hematopoiesis. Mol Cancer. 2020;19(1):5.

40. Black JC, Mosley A, Kitada T, Washburn M, Carey M. The SIRT2 deacetylase regulates autoacetylation of p300. Mol Cell. 2008;32(3):449–55.

41. Han Y, Jin YH, Kim YJ, Kang BY, Choi HJ, Kim DW, et al. Acetylation of Sirt2 by p300 attenuates its deacetylase activity. Biochem Biophys Res Commun. 2008;375(4):576–80.

42. Bachman M, Uribe-Lewis S, Yang X, Burgess HE, Iurlaro M, Reik W, et al. 5-Formylcytosine can be a stable DNA modification in mammals. Nat Chem Biol. 2015;11(8):555–7.

43. Bachman M, Uribe-Lewis S, Yang X, Williams M, Murrell A, Balasubramanian S. 5-Hydroxymethylcytosine is a predominantly stable DNA modification. Nat Chem. 2014;6(12):1049–55.

44. Zhang QQ, Zhang WJ, Chang S. HDAC6 inhibition: a significant potential regulator and therapeutic option to translate into clinical practice in renal transplantation. Front Immunol. 2023;14:1168848.

45. Li T, Zhang C, Hassan S, Liu X, Song F, Chen K, et al. Histone deacetylase 6 in cancer. J Hematol Oncol. 2018;11(1):111.

46. Grandi FC, Modi H, Kampman L, Corces MR. Chromatin accessibility profiling by ATAC-seq. Nat Protoc. 2022;17(6):1518–52.

Zamperla *et al. Clinical Epigenetics*   (2024) 16:109

Page 20 of 20

47. Jo H, Shim K, Jeoung D. Targeting HDAC6 to overcome autophagy-promoted anticancer drug resistance. Int J Mol Sci. 2022;23(17):9592.
48. Aguilar-Medina M, Avendano-Felix M, Lizarraga-Verdugo E, Bermudez M, Romero-Quintana JG, Ramos-Payan R, et al. SOX9 stem-cell factor: clinical and functional relevance in cancer. J Oncol. 2019;2019:6754040.
49. Yang W, Feng Y, Zhou J, Cheung OK, Cao J, Wang J, et al. A selective HDAC8 inhibitor potentiates antitumor immunity and efficacy of immune checkpoint blockade in hepatocellular carcinoma. Sci Transl Med. 2021;13(588):6804.
50. Vanaja GR, Ramulu HG, Kalle AM. Overexpressed HDAC8 in cervical cancer cells shows functional redundancy of tubulin deacetylation with HDAC6. Cell Commun Signal. 2018;16(1):20.
51. Iida M, Harari PM, Wheeler DL, Toulany M. Targeting AKT/PKB to improve treatment outcomes for solid tumors. Mutat Res. 2020;819–820: 111690.
52. Pascual J, Turner NC. Targeting the PI3-kinase pathway in triple-negative breast cancer. Ann Oncol. 2019;30(7):1051–60.
53. Jin Q, Yu LR, Wang L, Zhang Z, Kasper LH, Lee JE, et al. Distinct roles of GCN5/PCAF-mediated H3K9ac and CBP/p300-mediated H3K18/27ac in nuclear receptor transactivation. EMBO J. 2011;30(2):249–62.
54. Wang M, Chen Z, Zhang Y. CBP/p300 and HDAC activities regulate H3K27 acetylation dynamics and zygotic genome activation in mouse preimplantation embryos. EMBO J. 2022;41(22): e112012.
55. Cai LY, Chen SJ, Xiao SH, Sun QJ, Ding CH, Zheng BN, et al. Targeting p300/CBP attenuates hepatocellular carcinoma progression through epigenetic regulation of metabolism. Cancer Res. 2021;81(4):860–72.
56. Benedetti R, Conte M, Iside C, Altucci L. Epigenetic-based therapy: from single- to multi-target approaches. Int J Biochem Cell Biol. 2015;69:121–31.
57. Kaur S, Rajoria P, Chopra M. HDAC6: a unique HDAC family member as a cancer target. Cell Oncol (Dordr). 2022;45(5):779–829.

Publisher's Note